Geophys. J. Int. (2000) **140,** 687–697

Melt migration beneath mid-ocean ridges

Abdolreza Ghods and Jafar Arkani-Hamed

Earth and Planetary Sciences, McGill University, 3450 *University Street, Montreal, Quebec,* H3A 2A7, *Canada. E-mail: jafar@planet.eps.mcgill.ca*

Accepted 1999 October 1. Received 1999 September 30; in original form 1999 January 11

SUMMARY

Using a two-phase flow model, we investigate the formation of a high-percentage melt layer beneath the oceanic lithosphere and focusing of the melt towards the ridge axis, taking into account freezing and melt extraction. Melt migration is modelled dynamically within a viscous permeable media that includes the asthenosphere and viscous part of the lithosphere. Due to a much faster melt migration in the brittle part of the lithosphere, the melt migration is simulated by instantaneous melt extraction from an assigned melt extraction region beneath the ridge axis. It is shown that a high-percentage melt layer forms and successfully focuses melt to a narrow zone beneath the mid-ocean ridge. Performance of the melt focusing mechanism is not significantly sensitive to the size of the melt extraction region, the melt extraction threshold and the spreading rate. In all of our models, about half of the total melt production freezes beneath the base of the lithosphere and the rest is focused towards the ridge and forms the crust.

Key words: flow model, lithosphere, melt migration, mid-ocean ridges.

INTRODUCTION

Oceanic crust forms within a 1–2 km wide neovolcanic zone at mid-ocean ridge at all spreading rates (e.g. Macdonald 1984). Two categories of models have been proposed to explain the creation of this narrow zone: those in which mantle flow is focused and a narrow high-percentage partially molten zone is created directly beneath the ridge axis (e.g. Rabinowicz *et al.* 1984; Whitehead *et al.* 1984; Crane 1985; Buck & Su 1989; Cordery & Phipps Morgan 1993; Barnouin-Jha & Parmentier 1997); and those in which melt from a wide, low-percentage, partially molten zone is focused on a narrow region beneath the ridge axis (e.g. Phipps Morgan 1987; Nicolas 1990; Sparks & Parmentier 1991, 1994; Aharonov *et al.* 1995; Kelemen & Dick 1995; Kelemen *et al.* 1995a,b). The recent multidisciplinary Mantle Electromagnetic and Tomography (MELT) experiment (Forsyth *et al.* 1998) favours the second category, showing that the partially molten zone beneath the fast spreading centre of the East Pacific Rise is a few hundred kilometres wide with a melt concentration of the order of 1–2 per cent. These findings emphasize the need for an understanding of how melt migrates from a wide, partially molten region and focuses itself on the narrow neovolcanic zone.

The first category of models assumes that compaction/decompaction of partially molten upper mantle has an insignificant effect on the dynamics of mantle flow and melt focusing, because the compaction/decompaction length is considerably smaller than the length scale for major changes in melt concentration (Ribe 1985). Consequently, melt is extracted at a steady rate from the partially molten zone without considering the possible formation of a decompacting layer or partial freezing of melt beneath the lithosphere.

The second category of models includes Sparks & Parmentier's (1991) model, which suggests that the excess pressure of melt near the bottom of the subsolidus lithosphere causes the melt to collect into a thin layer and form a layer of high-percentage melt beneath the sloping base of the impermeable lithosphere (similar to the decompacting layer of our models). Based on steady-state 1-D calculations, Sparks & Parmentier (1991, 1994) suggested that the melt within the layer partially freezes and the rest is effectively focused towards the ridge. Spiegelman (1993) investigated the formation of a decompacting layer beneath a freezing front using 1-D numerical models and showed that the decompaction significantly affects the melt distribution over many compaction lengths. The stability and focusing ability of the decompacting layer in realistic conditions of melting, freezing and melt extraction along a 2-D mid-ocean ridge is a fundamental problem that requires detailed investigation.

Amongst other mechanisms in the second category of the models are hydrofracturing (Nicolas 1990), stress-induced anisotropic permeability (Phipps Morgan 1987) and reaction–infiltration instability (Aharonov *et al.* 1995; Kelemen & Dick 1995; Kelemen *et al.* 1995a,b). Geological evidence suggests that hydrofracturing is limited to depths above the brittle–ductile transition zone. Dykes extending into the mantle section of ophiolites mostly form off axis, away from the mid-ocean ridge axis, near the brittle–ductile transition, and above the

adiabatically ascending partially molten mantle (Kelemen & Dick 1995; Kelemen *et al.* 1995b). The second mechanism suggests that the accumulated strain associated with passive mantle flow beneath the spreading centre results in an anisotropic permeability, so that melt can be effectively focused within the neovolcanic zone even in a lower-viscosity upper mantle. The magnitude of the permeability enhancement has yet to be determined and it is still not clear whether the pressure gradient arising from mantle flow with a viscosity of less than 10^{21} Pa s is sufficient to direct melt towards the ridge. The third theory considers the partially molten upper mantle as a reactive, permeable compacting/decompacting two-phase fluid media, and suggests that the positive feedback between rate of dissolution and permeability further increases the permeability caused by local melt-induced dissolution along melt migration paths. This may result in the lateral convergence of melt into the high-permeability fingers (Kelemen *et al.* 1995a). However, it is not yet known at what depth beneath the mid-ocean ridge melt migration through high-permeability fingers becomes more significant than the upward porous mantle flow. In this study we assume that there is no reaction between the solid matrix and migrating melt and we investigate the role of physical compaction/decompaction of the partially molten upper mantle on focusing of melt beneath mid-ocean ridges. We regard this as a step towards a more realistic model that may include reaction–infiltration instability.

Using a two-phase flow model, we explore the possibility of the formation of a high-percentage melt layer and its ability to focus melt towards the ridge. The models presented in this paper consist of three components: lithosphere, asthenosphere and a melt extraction region. Fig. 1 schematically displays a cross-section of a spreading centre with a broad low-percentage partially molten region. The melt migrates vertically within the partially molten zone and moves laterally within the decompacting layer up the slope towards the ridge axis. The lithosphere is defined using a temperature-dependent viscosity and is considered to be impermeable everywhere except within the melt extraction region. In the asthenosphere, melt migrates under the influence of its buoyancy and pressure gradient arising from compaction/decompaction and mantle flow. The melt extraction region represents the brittle upper part of the lithosphere where melt velocity is very fast. To simulate the fast melt migration, melt is extracted instantaneously from the melt extraction region whenever melt fraction exceeds a specified threshold. The sensitivity of the melt extraction mechanism to the size of the melt extraction region is evaluated by using two melt extraction regions 5 km wide by 6.4 km deep and 10 km wide by 10 km deep. Likewise, the effect of the melt extraction threshold is investigated using two melt extraction thresholds of 2.5 and 5 per cent. We show that the high-percentage melt layer can form and focus melt within a region a few kilometres wide beneath the mid-ocean ridge, and that crustal production is not significantly sensitive to either the size of the melt extraction region or the threshold of melt extraction.

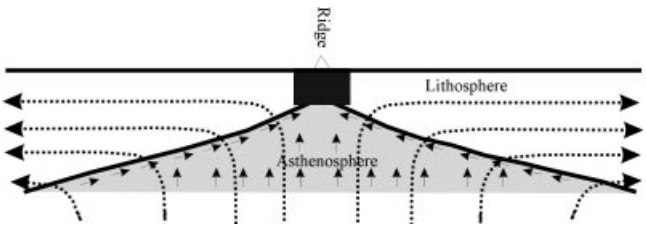

Figure 1. A schematic cross-section of a spreading centre with a broad partially molten zone. Melt migrates vertically within the partially molten zone and laterally towards the ridge at the top of the partially molten zone. The dashed lines are streamlines. The black rectangle shows the melt extraction region.

NUMERICAL MODEL

The upper mantle rocks ascend beneath spreading centres primarily in response to the horizontal motion of the overlying plates and secondarily due to their thermal, chemical and melt retention buoyancy forces. We model the corner flow induced by seafloor spreading in a computational frame 600 km wide and 200 km deep (Fig. 2) while considering all of the buoyancy forces. Our boundary conditions (Fig. 2) are similar to those of Cordery & Phipps Morgan (1993) and Jha *et al.* (1994). The top boundary moves horizontally with a specified spreading velocity of U_c. Mass is allowed to enter vertically from the bottom boundary and exit horizontally from the right boundary. The top and left boundaries are impermeable. Temperature is fixed at the top and bottom boundaries to zero and T_b, respectively. Three different values of T_b—1350, 1425 and 1450 °C—are used in different models. Zero thermal and melt flux boundary conditions are used across the left and right boundaries. The initial temperature field is that of a cooling half-space modified using a melting model, where the initial temperature field is corrected to account for the latent heat of melting. Partial melting depletes solid matrix residue by

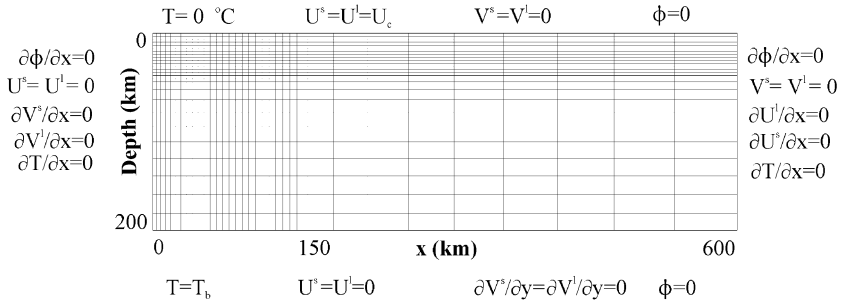

Figure 2. The grid and boundary conditions used in our models. For clarity, in each direction only one node out of six is shown in the figure. Resolution is high within an area 50 km from the surface and 150 km from the ridge axis. U^s and U^l are the horizontal components of the solid matrix and melt velocities and V^s and V^l are the vertical components. U_c is the assigned half-spreading rate. x and y are the horizontal and vertical coordinate axes, where y increases with depth from the surface.

removing components with low solidus temperatures. We specify the solid residue by a depletion field $\mathscr{M}$ that specifies what ratio of the pristine rock should melt to produce the solid residue. For example, $\mathscr{M}=0.2$ is a solid residue resulting from 20 per cent partial melting. The initial depletion field is set to the initial partial melting, and the initial melt fraction field ϕ is set to zero to reduce time-dependent behaviour of the system that arises solely from the initial conditions. The initial complete extraction of the melt does not affect our results because we are interested in the steady-state conditions of our models. A temperature-dependent Arrenhius-type viscosity,

$$\eta_s = C_0 \exp\left(\frac{E}{R\,(T+273)}\right), \tag{1}$$

is adopted, where R, E and T are the universal gas constant, the activation energy and the temperature. Temperature is expressed in degrees Celsius throughout the paper. C_0 is determined by setting a reference viscosity of $\eta_s^0 = 1.\times 10^{19}$ Pa s at 200 km depth, the bottom of our computational domain. This reference viscosity value is selected in accordance with previous studies (e.g. Sotin & Parmentier 1989; Cordery & Phipps Morgan 1993), which thoroughly investigated the effect of a constant and a pressure–temperature-dependent viscosity on the total melt production, and showed that a viscosity of $1.\times 10^{19}$ Pa s results in a crustal production that weakly depends on spreading rate. Viscosities larger than 500 η_s^0 are set to 500 η_s^0, resulting in an almost rigid lithosphere that moves with the assigned spreading velocity. In this study we do not consider the effect of the melt fraction (Hirth & Kohlstedt 1995a,b) and hydrogen fugacity (Hirth & Kohlstedt 1996) on the viscosity of the solid matrix. Permeability is considered to be a function of melt fraction,

$$K_\phi = 10^{-3} a^2 \phi^3, \tag{2}$$

where a is the grain size (Von Bargen & Waff 1986; Cheadle 1993). Eq. (2) implicitly assumes that the porosity network is interconnected at all melt fractions, which is in good agreement with experimental results (Kohlstedt 1992). The physical parameters used in this paper are listed in Table 1.

We solve the equations of conservation of mass, momentum and energy for a two-phase flow model. The equations are based on McKenzie's (1984) derivations, modified to take into account the effect of melt extraction. The model consists of two incompressible media, a continuous and permeable solid matrix and melt that flows through the matrix. A given partially molten region compacts if melt migrates out, and decompacts if melt migrates in from elsewhere. The non-dimensionalized governing equations, using Einstein's summation rule, are

$$-\phi_0 \frac{\partial \phi}{\partial t} + \frac{\partial}{\partial x_i}\left((1-\phi_0\phi) V_i^s\right) = 0, \tag{3}$$

$$\phi_0 \frac{\partial \phi}{\partial t} + \frac{\partial}{\partial x_i}\left(\phi_0 \phi V_i^l\right) = \Gamma_e, \tag{4}$$

$$\frac{\partial \Pi}{\partial x_i} = \frac{\partial}{\partial x_j}\left((1-\phi_0\phi)\left(\zeta \frac{\partial V_k^s \delta_{ij}}{\partial x_k} + \tau_{ij}^s\right)\right) + Ra((\rho_s - \rho_s^0) + \phi_0\phi(\rho_s - \rho_l))\delta_{i3}, \tag{5}$$

$$\tau_{ij} = \eta_s\left[\frac{\partial V_i^s}{\partial x_j} + \frac{\partial V_j^s}{\partial x_i} - \frac{2}{3}\,\delta_{ij}\,\frac{\partial V_k^s}{\partial x_k}\right], \tag{6}$$

$$V_i^l - V_i^s = -D\,\frac{K_\phi}{\phi}\left(\frac{\partial \Pi}{\partial x_i} + Ra(1-\rho_l)\delta_{i3}\right) \tag{7}$$

and

$$\rho_s C_P \frac{\partial T}{\partial t} + \rho_s C_P((1-\phi_0\phi)V_i^s + \phi_0\phi V_i^l)\frac{\partial T}{\partial x_i} = \frac{1}{Pe}\,\frac{\partial}{\partial x_i}\left(K\frac{\partial T}{\partial x_i}\right) + \Gamma_e T. \tag{8}$$

The notation is defined in Table 2 and The normalization schemes are listed in Table 3, where the normalized variables are asterisked. The asterisks are omitted in the above equations for clarity. x_i and t are coordinate axes and time. V_i^s, V_i^l, τ^s and Π are the solid matrix velocity, melt velocity, shear stress of the solid matrix and reduced pressure, respectively. Pressure is defined as $P = \Pi + \rho_s^0 g \delta_c \delta_{i3}$, where g and ρ_s^0 are the gravity and reference density of the solid matrix. δ_c is the characteristic length over which compaction occurs and is called the compaction length. It is assumed that any pressure difference between the solid matrix and the melt leads to an instantaneous volumetric deformation. For example, compaction occurs if the solid matrix pressure is larger than the melt pressure. The difference between the solid matrix and the melt pressure, ΔP, is related to a linear volumetric deformation of the solid matrix by $\Delta P = \zeta \partial V_k^s / \partial x_k$. ζ is the bulk viscosity of the two-phase flow media, which is assumed to be equal to the viscosity of the solid matrix. ϕ, ϕ_0 and K_ϕ are the melt fraction, the reference melt fraction and the permeability. ρ_s, ρ_l, C_P and K are the density of the solid matrix, the density of the melt, the specific heat and the thermal conductivity. δ_{ij} is the Kronecker delta function. Γ_e is the rate of melt extraction; it is always zero outside the melt extraction region. Eqs (3) and (4) express the conservation of the solid matrix and the melt, where both the melt and the solid matrix densities are assumed to be constant. The density of the solid matrix (ρ_s) is not, however, constant in the momentum equation for the solid matrix, (eq. 5). It is a function of temperature and the depletion induced by melting,

$$\rho_s = \rho_s^0(1 - \alpha(T - T_0) - \beta\mathscr{M}), \tag{9}$$

where α and β are the coefficients of thermal and depletion expansion, respectively. T_0 is the reference temperature, assumed to be the average of the temperatures at the top and bottom of the computational domain. Eq. (6) is the stress–strain constitutive law for a compressible media. Eq. (7) is

Table 1. Physical parameters used in this paper.

Parameter	Value
Reference solid density (ρ_s^0)	3300 kg m^{-3}
Reference melt density (ρ_l^0)	2800 kg m^{-3}
Earth gravity (g)	9.8 m s^{-2}
Reference viscosity of solid (η_s^0)	1×10^{19} Pa s
Viscosity of melt (η_l)	1 Pa s
Thermal conductivity (K)	3.3 W m $^\circ$C^{-1}
Specific heat (C_P)	1000 J kg^{-1} $^\circ$C^{-1}
Grain size (a)	1 cm
Latent heat of melting (H)	1.2×10^9 J m^{-3}
Thermal expansion coefficient (α)	3×10^{-5} $^\circ$C^{-1}
Depletion expansion coefficient (β)	0.024[1]
Activation energy (E)	3×10^5 J mol^{-1}
Universal gas constant (R)	8.314 J mol^{-1} $^\circ$C^{-1}

[1] Sparks & Parmentier 1994.

Table 2. Notation.

Variable	Description	Units
C_P	specific heat at constant pressure	J kg^{-1} °C^{-1}
C_P^{s}	specific heat of solid at constant pressure	J kg^{-1} °C^{-1}
C_P^{l}	specific heat of melt at constant pressure	J kg^{-1} °C^{-1}
δ_{c}	compaction length	m
ΔT	temperature drop across the computational domain	°C
E	activation energy	J mol^{-1}
g	gravitational acceleration	m s^{-2}
H	latent heat of melting	J m^{-3}
K_ϕ	permeability	m^2
K	thermal conductivity	W m^{-1} °C^{-1}
$\mathscr{M}$	depletion factor	–
P	pressure	Pa
P_{H}	hydrostatic pressure	Pa
Π	reduced pressure	Pa
Pe	Peclet number	–
R	universal gas constant	J mol^{-1} °C^{-1}
Ra	buoyancy to viscous force ratio	–
T	temperature	°C
t	time	s
V_i^{s}	solid matrix velocity	m s^{-1}
V_i^{l}	melt velocity	m s^{-1}
W^0	reference vertical velocity component for melt	m s^{-1}
x_i	coordinate axes	m
α	thermal expansion coefficient	°C^{-1}
β	depletion expansion coefficient	–
η_{s}	shear viscosity of solid matrix	Pa s
η_{s}^0	reference shear viscosity of solid matrix	Pa s
η_{l}	shear viscosity of liquid	Pa s
Γ_{e}	rate of melt extraction	s^{-1}
ζ	bulk viscosity of solid matrix	Pa s
κ_{s}^0	reference solid matrix diffusivity	m^2 s^{-1}
ϕ	volumetric percentage of melt	–
ϕ_0	reference volumetric percentage of melt	–
ρ_{s}	density of solid matrix	kg m^{-3}
ρ_{l}	density of liquid	kg m^{-3}
ρ_{s}^0	reference mantle density	kg m^{-3}

Table 3. Normalization schemes.

$W_0 = \dfrac{K_\phi^0}{\eta_{\mathrm{l}}}(1-\phi_0)(\rho_{\mathrm{s}}-\rho_{\mathrm{l}})g$	$\delta_{\mathrm{c}} = \left[\dfrac{K_\phi^0(\zeta+4\eta_{\mathrm{s}}^0/3)}{\eta_{\mathrm{l}}}\right]^{1/2}$	$x_i = x_i^* \delta_{\mathrm{c}}$
$t = \dfrac{\delta_{\mathrm{c}}}{W_0}\, t^*$	$V_i^{\mathrm{s}} = W_0 V_i^{\mathrm{s}*}$	$V_i^{\mathrm{l}} = W_0 V_i^{\mathrm{l}*}$
$\Pi = \dfrac{\eta_{\mathrm{s}}^0 W_0}{\delta_{\mathrm{c}}}\,\Pi^*$	$T = \Delta T\ T^*$	$\rho_{\mathrm{s}} = \rho_{\mathrm{s}}^0 \rho_{\mathrm{s}}^*$
$\rho_{\mathrm{l}} = \rho_{\mathrm{s}}^0 \rho_{\mathrm{l}}^*$	$\eta_{\mathrm{s}} = \eta_{\mathrm{s}}^0 \eta_{\mathrm{s}}^*$	$\zeta = \eta_{\mathrm{s}}^0 \zeta^*$
$\kappa_{\mathrm{s}}^0 = \dfrac{K}{\rho_{\mathrm{s}}^0 C_P^{\mathrm{s}}}$	$K_\phi = K_\phi^0 K_\phi^*$	$K_\phi^0 = 10^{-3} a^2 \phi_0^3$

the momentum equation for the melt, which is equivalent to Darcy's law. In the momentum equations the non-dimensional number $Ra = \rho_{\mathrm{s}}^0 g \delta_{\mathrm{c}}^2/(\eta_{\mathrm{s}}^0 W_0)$ is similar to the conventional Rayleigh number in that it describes the relative strength of mantle buoyancy force versus the viscous force. W_0 is the characteristic velocity of the melt. The second non-dimensional number, $D = \eta_{\mathrm{s}}^0 K_\phi^0/(\eta_{\mathrm{l}}\phi_0\delta_{\mathrm{c}}^2)$, denotes the efficiency of melt migration. K_ϕ^0 and η_{l} are the reference permeability of the solid matrix and the viscosity of the melt. Eq. (8) is the conservation of energy equation. The non-dimensional Peclet number, $Pe = W_0\delta_{\mathrm{c}}/\kappa_{\mathrm{s}}^0$, describes the ratio of the rate of thermal advection to that of thermal diffusion, where κ_{s}^0 is the thermal diffusivity of the melt and solid matrix. In writing the energy equation, it is implicitly assumed that a thermal equilibrium exists between the melt and the solid matrix. We also assume that $\rho_{\mathrm{l}} C_P^{\mathrm{l}} = \rho_{\mathrm{s}} C_P^{\mathrm{s}}$, where C_P^{s} and C_P^{l} are the specific heat of the solid matrix and the melt.

An iterative finite volume method (Patankar 1980) is adopted to solve eqs (3)–(8). A second-order Runge–Kutta method is used for discretization of the time derivatives in the equations of conservation of melt (eq. 4) and energy (eq. 8). To calculate the pressure field, eqs (3) and (4) are combined and converted to a pressure equation using the momentum equations, which is then solved by the SIMPLER method (Prakash & Patankar 1985). This eliminates the time derivative terms and yields a pressure equation with no explicit time dependence. The numerical results presented in this paper are calculated in a non-uniform rectangular grid with 211×161 nodes (Fig. 2), with a high-resolution area at 50 km depth and 150 km away from the ridge axis where melt percentages are usually high and a decompacting layer forms beneath the lithosphere. The vertical grid spacing within the high-resolution area is 0.5 km; outside this region it varies between about 0.9 and 3 km. The horizontal grid spacing within the high-resolution area is about 0.3 km close to the ridge axis and increases away from the ridge axis to a maximum of about

1.2 km. The horizontal resolution outside the high-resolution area increases from 1.5 to 10 km away from the axis. The variable grid reasonably resolves both compaction δ_c and freezing δ_f length scales involved in our problem. δ_c is always larger than 1.52 km for $\phi > 0.01$. According to Spark & Parmentier's (1994) calculations, δ_f is about 3 and 0.6 km for spreading rates of 10 and 50 km Myr^{-1}, respectively.

MELTING, FREEZING AND MELT EXTRACTION

We use a dynamical melting model (Ghods & Arkani-Hamed 1998) where some portion of melt may remain with the matrix, some part may migrate out, or some extra melt may be added to a given volume in the partially molten zone by melt migration from elsewhere. $\mathscr{M}$ is smaller than ϕ in the regions where melt accumulates and larger than ϕ in the regions where melt is removed. Our dynamical melting model is a modified version of McKenzie & Bickle's (1988) batch melting model and is constructed by replacing the liquidus temperature of peridotite by the liquidus temperature of pure forsterite (i.e. $T_l^0 = 2164 + 4.77 P_H$; Presnall & Walter 1993). Furthermore, to account for the dynamic nature of the problem, the $\mathscr{M}$ field is advected in each time step using the following pure advective transport equation:

$$\frac{\partial \mathscr{M}}{\partial t} + V_i^s \frac{\partial \mathscr{M}}{\partial x_i} = 0 . \tag{10}$$

The above equation is solved using the monotonic second-order upwind method (Sweby 1984). The fraction of melt produced in a given time step, $\Delta\mathscr{M}$, is computed using the following coupled equations,

$$\rho_s C_P T_1 = \rho_s C_P T_2 + \Delta\mathscr{M} H , \tag{11}$$

$$\Delta\mathscr{M} = \frac{T_2 - T_s}{T_l^0 - T_s} (1 - \mathscr{M}) , \tag{12}$$

where T_1 and T_2 are the temperatures before and after correction, respectively, and the latent heat of melting H is considered to be constant. T_s is the instantaneous solidus temperature of the solid residue and increases with progressive melting. T_s is calculated in a given time step using $\mathscr{M} = T - T_s^0/(T_l^0 - T_s^0)$ and setting $T_s = T$, where T_s^0 is the solidus temperature of pristine dry peridotite. The latter is done to account for the increase of T_s through melting. The removal of the melt in a fractional melting model increases T_s because the residue becomes more refractory. The temperature field is corrected for the absorption of the latent heat of melting and $\Delta\mathscr{M}$ is added to the ϕ and $\mathscr{M}$ fields to obtain new melt fraction and depletion distributions.

Freezing of melt beneath the cold impermeable lithosphere is considered. Assuming that the chemical reactions governing the partial melting are reversible, the procedure described for the calculation of partial melting is equally applicable for the calculation of partial freezing. The only modification is when the computed fractional freezing is larger than the existing melt fraction in a given partially molten control volume, where we allow complete freezing and further reduce the temperature below the solidus temperature to conserve the total thermal energy within the control volume. Therefore, the maximum freezing is limited to the melt fraction present in the control volume. The freezing model is very simple and straightforward to implement in the numerical model; however, it defies the fact that freezing is not the reversal of the melting process (Kelemen *et al.* 1995b). We will address the possible consequences of this shortcoming in the Discussion.

In contrast to the slow melt flow within the partially molten porous zone of the upper mantle, melt migrates much faster via fractures and veins within the brittle upper part of the lithosphere (e.g Nicolas 1990; Ceuleneer & Rabinowicz 1992). We simulate the fast melt migration by considering a melt extraction region beneath the mid-ocean ridge axis. Melt is extracted from the region instantaneously whenever it exceeds a specified threshold. Melt extraction compacts the partially molten regions, and enhances the mantle upwelling velocity, the rate of melting and the crustal production. The dynamical and thermal effects associated with melt extraction are included in the modelling by adding the rate of melt extraction, Γ_e, to the equation of conservation of melt (eq. 4) and the corresponding rate of extraction of thermal energy, $\rho_l C_P^l \Gamma_e T$, to the energy equation (eq. 8). In the energy equation, this term appears as $\Gamma_e T$ because the equation is non-dimensionalized and it is assumed that $\rho_l C_P^l = \rho_s^0 C_P^s$, as mentioned above. Γ_e is either zero or negative.

Our investigation showed that including the rate of melt extraction in a model with melt migration but without allowing for freezing increases the crustal production by about 16 per cent or about 1 km. Cordery & Phipps Morgan (1992) reported a larger increase of 33 per cent or 2 km. This is because we extracted melt only from a narrow melt extraction region, whereas they extracted melt from the top of a wide partially molten zone. A wide melt extraction region results in a larger increase of mantle upwelling velocity and thus crustal production than a narrow melt extraction region.

The size of the melt extraction region is a matter of uncertainty, and is investigated in this paper. Numerous lines of evidence suggest that the melt migration within the sub-solidus lithosphere and even in the top portion of the partially molten zone is strongly controlled by the permeability induced by the formation of cracks and veins (Nicolas 1990; Ceuleneer & Rabinowicz 1992; Turcotte & Phipps Morgan 1992; Korenaga & Kelemen 1997; Kelemen & Aharonov 1998). The existence of dykes in the middle crust is indicative of the presence of rock rupturing at those depths (Turcotte, & Phipps Morgan 1992). For lower crustal depths, melt accumulation beneath a permeability barrier such as the lithosphere may induce crack propagation driven by overpressure and melt buoyancy (Korenaga & Kelemen 1997; Kelemen & Aharonov 1998). Furthermore, ophiolite studies suggest the presence of fractures and Metre-scale veins within the upper mantle at the top of the partially molten zone (e.g. Nicolas 1990; Ceuleneer & Rabinowicz 1992).

MODELLING

In the first set of experiments, we examine the fidelity of our models by reproducing the previous models of Sotin & Parmentier (1989). The crustal thickness is computed at different spreading rates for a model that does not consider freezing, uses Sotin & Parmentier's (1989) batch melting model and has a basal temperature of 1350 °C. Similar to Sotin & Parmentier's (1989) models, melt is extracted completely, a constant viscosity is used and only chemical buoyancy forces

are considered. The crustal production calculated by our models for half-spreading rates of 10, 25 and 50 km Myr^{-1} are 7.7, 8.4 and 8.75 km, respectively, whereas those calculated using Sotin & Parmentier's (1989) models are 6.8, 7.5 and 8 km. Our computed crustal productions show a larger crustal thickness but their spreading rate dependence is very similar to that of Sotin & Parmentier's (1989) models. We also compute the crustal thickness at different spreading rates. Melt is allowed to migrate vertically and is extracted instantaneously from the top of the partially molten zone without allowing lateral melt migration or freezing. The crustal production calculated using our models for half-spreading rates of 10, 25 and 50 km Myr^{-1} are 5, 5.7 and 6 km, respectively, which are within the range of results reported from the similar models of Cordery & Phipps Morgan (1993).

We run a set of experiments for different basal temperatures (T_b) while allowing freezing in order to determine a basal temperature that produces the observed thickness of the oceanic crust. In the next step, we explore the performance of the melt extraction mechanism at different melt extraction criteria and spreading rates through two sets of experiments using the successful basal temperature. The melt extraction criteria, the size of the melt extraction region and the melt extraction threshold are assumed to be adjustable variables in this modelling. The sensitivity of the melt extraction mechanism is investigated for different melt extraction criteria at a fixed half-spreading rate of 50 km Myr^{-1} The successful model from these experiments is then used to evaluate the spreading rate dependence of the melt extraction mechanism.

An acceptable model is one that satisfies two observations, namely a crustal production that weakly depends on spreading rate and a very narrow zone of crustal emplacement. Except for half-spreading rates below 10 km Myr^{-1}, the thickness of the oceanic crust is essentially independent of spreading rate (Chen 1992). Geomorphological and geological studies of mid-ocean ridges show that 90 per cent of the oceanic crust is emplaced within a 1–2 km wide neovolcanic zone at all spreading rates (Macdonald 1984). The narrow crustal low-velocity zone beneath fast spreading mid-ocean ridges is interpreted to be a high melt fraction zone (Harding *et al.* 1989; Vera *et al.* 1990; Sinton & Detrick 1992), and therefore a zone of crustal emplacement. The width of the low-velocity zone is about 1 km at the ridge and increases to 5–6 km (on either flank of the ridge) at the base of the crust, suggesting that the crustal emplacement zone remains within a few kilometres.

To evaluate the performance of our models we calculate crustal thickness, total melt production, total freezing and melt extraction efficiency. As we will show later, the crustal production, the total melt production and the total freezing have strong temporal variations, but the values reported in this paper are mean values calculated over the run time. The total melt production also includes the volume of melt that is frozen beneath the lithosphere. The crustal thickness is calculated by dividing the total volume of melt extracted during a given time step by a width corresponding to the spreading distance over that time step. The total melt production and total freezing are presented as thickness per unit crustal width in order to compare them with the crustal thickness. To be consistent with previous studies (e.g. Cordery & Phipps Morgan 1993; Barnouin-Jha & Parmentier 1997), the crustal thickness reported in this paper is not corrected for volumetric contraction due to solidification. The melt extraction efficiency is an approximate indicator of how much of the total melt production is extracted and how much is frozen. It is calculated by dividing the crustal thickness by the total melt production.

Basal temperature

To find the basal temperature required for the production of the observed oceanic crust, we run three experiments for basal temperatures of 1350, 1425 and 1450 °C, which are within the range of suggested temperatures at the top of the asthenosphere (Sclater & Parsons 1981; Stein & Stein 1992). Due to the small adiabatic temperature gradient in the upper mantle, the difference between the temperature at the top of the asthenosphere and that at the base of our models, 200 km, is not appreciable. A fixed half-spreading rate of 50 km Myr^{-1}, a melt extraction region 5 km wide and 6.4 km deep and a melt extraction threshold of 5 per cent are used in these models. Fig. 3 shows the total melt production, crustal thickness and total freezing for the different basal temperatures. The melt extraction efficiency of the models is around 50 per cent, indicating that almost half of the total melt produced freezes and the rest is extracted to produce the crust. A basal temperature of 1425 °C produces a crustal thickness of about 6.3 km, which is within the observed range of 6–7 km (Chen 1992). Crustal thickness significantly varies with time for models with basal temperatures of 1425 and 1450 °C. Fig. 4 shows the crustal production over time for a model with a basal temperature of 1425 °C. For clarity only part of the run time is shown. Due to our assigned zero initial melt fraction, crustal production increases with time in the early stages, but after about 0.1 Myr it reaches its characteristic oscillatory state with a mean period of about 0.009 Myr, varying between a minimum of zero and maximum of about 20 km. This large temporal variation is probably an artefact of our melt extraction method. The oscillations of the total melt production and freezing are in phase with the oscillations of the crustal production.

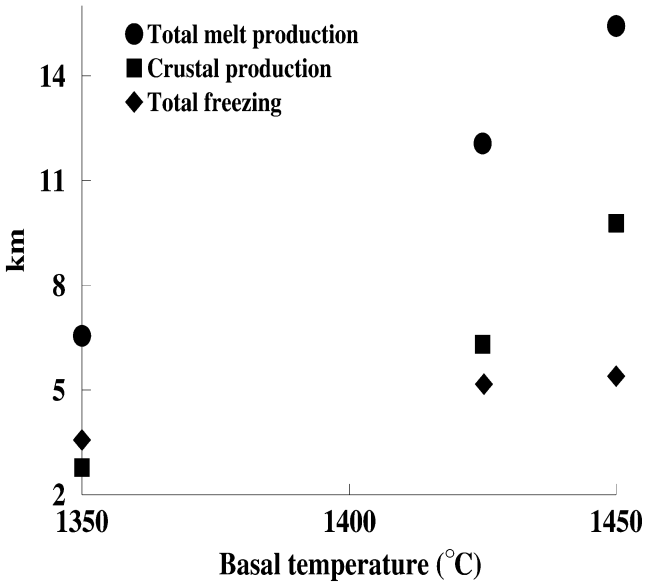

Figure 3. Total melt production, crustal production and total freezing versus basal temperature. A melt extraction threshold of 5 per cent, a melt extraction region 5 km wide by 6.4 km deep and a half-spreading rate of 50 km Myr^{-1} are employed in all of the models.

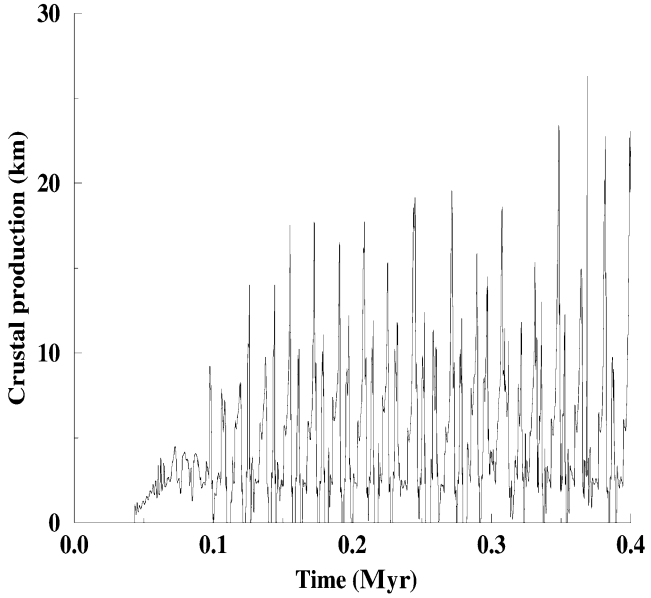

Figure 4. Temporal evolution of crustal production for a model with a basal temperature of 1425 °C and a spreading rate of 50 km Myr^{-1} For clarity only part of the run time is shown.

The melt fraction field of the model with a basal temperature of 1425 °C (Fig. 5a) shows a decompacting layer that forms beneath the sloping base of the lithosphere. The layer is composed of solitary waves that move up the slope towards the ridge axis. The thickness of the layer diminishes away from the ridge axis in response to progressively greater cooling of the lithosphere, more extensive freezing of the melt and a smaller rate of melt production away from the ridge. The melt fraction is at the specified maximum of 5 per cent beneath the ridge axis at depths between 1 and 5 km. This figure shows the formation of subhorizontal solitary waves within the partially molten region that ascend through the upper mantle primarily in response to their buoyancy forces, impact into the decompacting layer, and move along the sloping base of the lithosphere towards the ridge axis. The impact of the solitary waves induces oscillations in the thickness of the decompacting layer. The melt velocity field superimposed on Fig. 5(a) shows that melt partially moves towards the ridge axis within each of the solitary waves. This is because each of the solitary waves is surrounded by a less permeable layer at its top and bottom. The lateral migration of melt within a solitary wave results in an increase of the melt fraction close to the mid-ocean ridge. This in turn leads to the formation of instabilities, coalescence and changes in the slope of the solitary waves near the ridge axis. The local slope reversal of the solitary waves makes melt move away from the axis towards the larger melt fraction regions created by coalescence of the solitary waves, causing a further increase of the melt fraction in the coalesced region. A detailed investigation of the melt fraction field with time shows that the periods of peak crustal production (Fig. 4) are concurrent with the arrival of the coalesced regions of the solitary waves in the melt extraction region. The shapes and sizes of the coalesced regions change in a very complex way with time. This results in a strong temporal variation of melt delivery to the melt extraction region and thus a strong temporal variation of crustal production. Melt from the partially molten areas far from the ridge axis, where solitary waves are not present, percolates almost vertically and then flows laterally towards the ridge axis along the sloping bottom of the lithosphere (Fig. 5a). Melt partially freezes within the decompacting layer, causing a sharp reduction of the depletion field, $\mathscr{M}$, at the top of the partially molten zone between 2 and 18 km depth (Fig. 5b), which is referred to as the freezing layer hereafter. Only part of the freezing layer is shown in Fig. 5(b), delineated by dashed curves. Freezing refertilizes the depleted peridotites beneath the lithosphere and thus reduces $\mathscr{M}$.

Melt extraction criteria

To evaluate the sensitivity of the melt extraction mechanism to the size of the melt extraction region, we conduct two experiments using melt extraction regions 5 km wide by 6.4 km deep and 10 km wide by 10 km deep. The first extends from the surface to the base of the crust and the second extends to the top few kilometres of the partially molten zone. A fixed half-spreading rate of 50 km Myr^{-1} and a melt extraction threshold of 5 per cent are used. The mean crustal thickness and total melt production for both models are about 6.3 and 12.1 km, respectively. Rerunning the two models using a lower melt extraction threshold of 2.5 per cent yields similar results. This shows that the efficiency of the melt extraction mechanism is not significantly sensitive to the size of the melt extraction region or to the melt extraction threshold for a half-spreading rate of 50 km Myr^{-1}. Repeating the above experiments but for a spreading rate of 25 km Myr^{-1} shows that the efficiency of the melt extraction mechanism is not significantly sensitive to the melt extraction criteria. However, at a spreading rate of 10 km Myr^{-1}, the efficiency of the melt extraction mechanism becomes independent of the melt extraction criteria only if the depth of the melt extraction region exceeds 8 km.

Spreading rate

Spreading rate sensitivity of the melt extraction mechanism is investigated by repeating our successful model for two additional half-spreading rates of 10 and 25 km Myr^{-1}. A melt extraction region 5 km wide by 8 km deep is employed for the half-spreading rate of 10 km Myr^{-1} and a region 5 km wide by 6.4 km deep for half-spreading rates of 25 and 50 km Myr^{-1}. The thicker melt extraction region for the half-spreading rate of 10 km Myr^{-1} is in agreement with the observed thickening of the seismogenic zone beneath low spreading rate ridge axes (Huang & Solomon 1988). Fig. 6 shows the total melt production, the crustal thickness and the total freezing for the different spreading rates. The crustal production increases with the spreading rate and is about 3.2, 4.9 and 6.3 km for half-spreading rates of 10, 25 and 50 km Myr^{-1}, respectively. The melt extraction efficiency for half-spreading rates of 10, 25 and 50 km Myr^{-1} is about 30, 42 and 52 per cent, respectively. The efficiency reduces at lower spreading rates due to faster cooling of the lithosphere. Crustal production shows oscillatory characteristics for all three spreading rates, oscillating with a mean period of 0.04, 0.021 and 0.009 Myr for spreading rates of 10, 25 and 50 km Myr^{-1}, respectively.

Snapshots of the melt fraction fields for half-spreading rates of 10 and 25 km Myr^{-1} (Fig. 7) show a decompacting layer that formed beneath the sloping base of the lithosphere and solitary waves that formed within the partially molten area, similar to that of the model with a half-spreading rate of

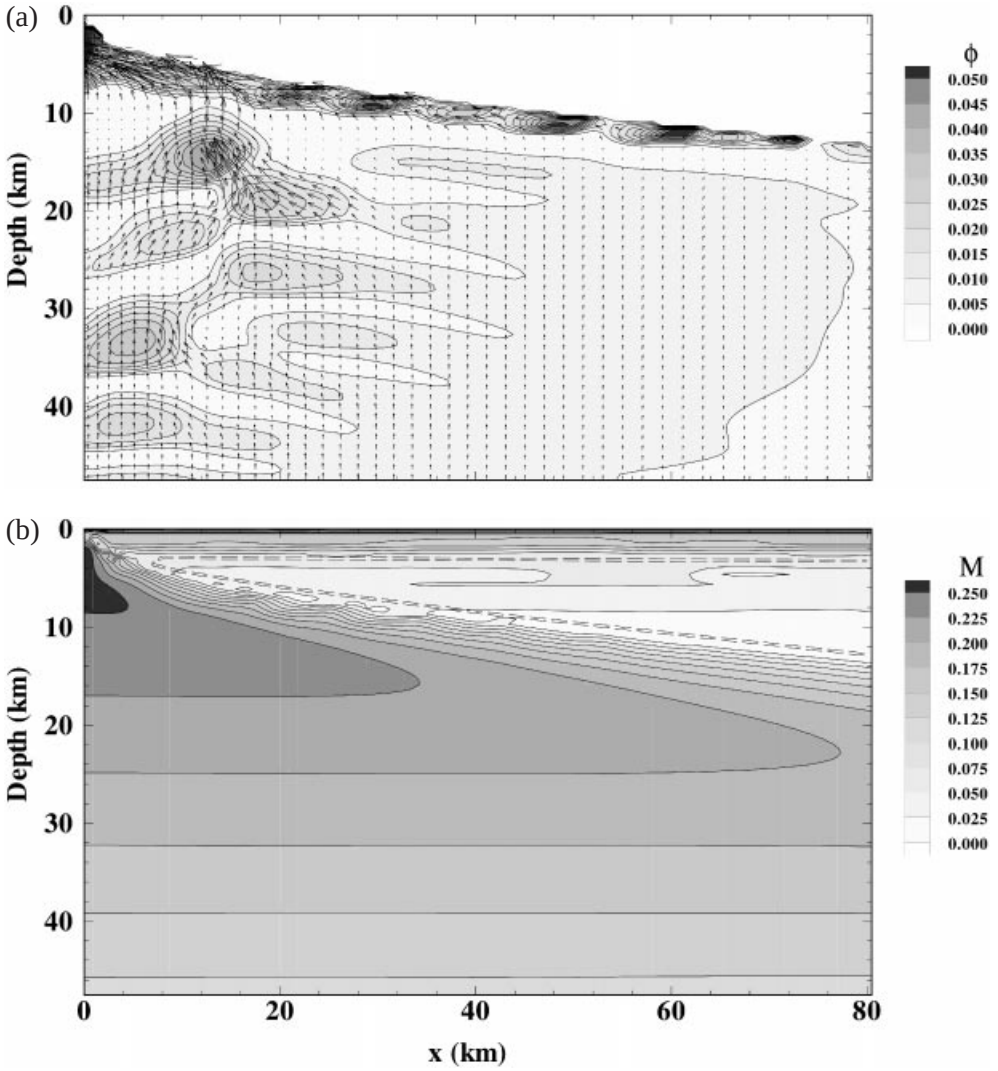

Figure 5. Snapshots of (a) the melt fraction and (b) the depletion fields for a half-spreading rate of 50 km Myr^{-1}. The melt velocity field is superimposed on (a). For clarity, only a quarter of the vector lines are shown in the melt velocity field. The dashed curve in (b) shows part of the freezing layer located close to the ridge axis. A basal temperature of 1425 °C, a melt extraction region 5 km wide by 6.4 km deep and a melt extraction threshold of 5 per cent are used. In this and the following figures, only the upper left corner of the computational domain is shown, and melt fraction and depletion fields are contoured at 0.005 and 0.025 intervals.

50 km Myr^{-1} (Fig. 5). The concentration of melt within the decompacting layer is at the specified maximum of 5 per cent close to the ridge axis. The faster cooling of the lithosphere at the slow half-spreading rate of 10 km Myr^{-1} reduces the width of the partially molten zone and makes the decompacting layer steeper and deeper by about 2 km at the ridge axis (Fig. 7a). Inspection of the corresponding depletion fields included in Fig. 7 reveals that the freezing layers for half-spreading rates of 10 and 25 km Myr^{-1} are located approximately at depth intervals of 14–31 and 9–22 km, respectively.

DISCUSSION AND CONCLUSIONS

We modelled melt migration below an oceanic ridge using a two-phase flow formulation and realistic conditions of melting, freezing and melt extraction. It is shown that the formation of a decompacting layer beneath the sloping base of an impermeable lithosphere is a viable mechanism for the focusing of melt beneath a narrow region below the neovolcanic zone at all spreading rates. Unlike previous models (e.g. Cordery & Phipps Morgan 1992, 1993; Barnouin-Jha & Parmentier 1997), the matrix is allowed to compact and decompact in response to melt removal and accumulation. Furthermore, freezing of the melt beneath the cold lithosphere is taken into account and melt is only extracted from a specified melt extraction region that includes mainly the crustal portion beneath the neovolcanic zone. The previous models allowed melt to migrate to the top of the partially molten zone and then instantaneously extracted it without considering any partial freezing or allowing any lateral melt migration towards the spreading centre.

Fast melt migration within the top brittle part of the lithosphere is simulated by extracting melt from a specified melt extraction region after the melt fraction exceeds a specified threshold. It is shown that the performance of the melt focusing mechanism and crustal production are not sensitive to the

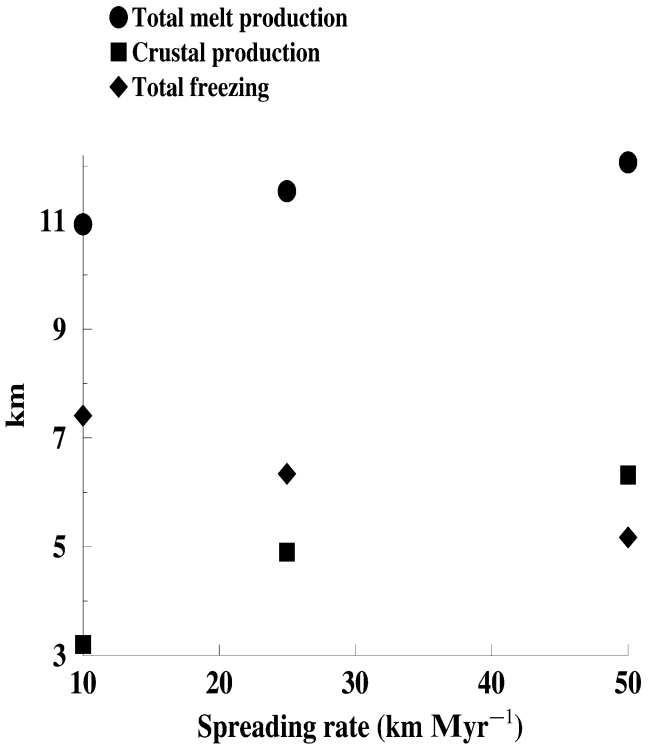

Figure 6. Total melt production, crustal production and total freezing versus half-spreading rate. A basal temperature of 1425 °C and a melt extraction threshold of 5 per cent are employed in all of the models. A melt extraction region 5 km wide by 6.4 km deep is used for the half-spreading rates of 25 and 50 km Myr^{-1} and a melt extraction region 5 km wide by 8 km deep for the half-spreading rate of 10 km Myr^{-1}.

size and threshold of the melt extraction region. Note that our melt extraction simulation implicitly assumes melt flux into the melt extraction region to be the only factor controlling the rate of melt extraction, and ignores the dynamics of crack formation. Cracks usually form when the pressure difference between the solid matrix and the melt, ΔP, becomes larger than the cohesive strength of the rocks. We cannot take crack formation into account because our continuum-based model cannot handle crack-related discontinuities.

Our models show that the crustal production is unsteady at all spreading rates. The mean periods of oscillations of crustal production for spreading rates of 10, 25 and 50 km Myr^{-1} are about 0.04, 0.021 and 0.009 Myr, respectively. The observed period of crustal production oscillations increases from 0.05 Myr for the fastest spreading rates to 1 Myr for the slowest ones (Tisseau & Tonnerre 1995). The predicted period of crustal production decreases with increasing spreading rate in agreement with observations; however, the periods are significantly larger than the observed ones. Furthermore, the amplitude of crustal thickness variations is unrealistically large. These discrepancies are probably related to our arbitrary melt extraction model, where melt is extracted from a pre-defined melt extraction region after exceeding a given threshold without considering the dynamics of crack formation within the brittle oceanic crust. Most probably, melt migrates within the crust in several stages before it erupts at the surface, causing longer-period magmatic events and smaller temporal variations of crustal thickness.

According to our models, at a spreading rate of 50 km Myr^{-1} about 50 per cent of the melt freezes at the top of the partially molten zone. Freezing increases at the lower spreading rates and reaches a maximum of about 70 per cent at a spreading rate of 10 km Myr^{-1}. This results in a low crustal production of 3.2 km at a spreading rate of 10 km Myr^{-1}. The spreading rate dependence of crustal production is directly related to our simplified freezing model, which assumes a complete reversibility of chemical reactions governing the partial melting and freezing. In general, freezing is not the reversal of melting, because decompression of high-temperature, high-pressure melt that migrated from a deeper part to a shallower depth changes the bulk compositions and phase relationships of the peridotite–melt mixtures within the partial melting region. This in turn results in the dissolution of some additional solids and hampers freezing beneath the cooling front (Kelemen *et al.* 1995b), and thus increases crustal production. Furthermore, contrary to the implicit assumption of batch crystallization made in our freezing model, crystallization may be fractional, so that increasingly evolved melts with lower solidus temperatures are formed. Such lower solidus temperature melts would freeze less beneath the impermeable lithosphere and thus increase crustal production and melt extraction efficiency further.

Our models (Figs 5 and 7) show that shallow-depth peridotites are slightly depleted because extensive freezing beneath the lithosphere refertilizes them. This observation is not in agreement with the observed highly depleted dredged mid-oceanic ridge peridotite samples (Johnson *et al.* 1990; Johnson & Dick 1992) and drilled samples in the Pacific (Dick & Natland 1996) and Atlantic oceans (Ross & Elthon 1996). The samples are highly depleted, probably by 10–20 per cent melting. This discrepancy between our model prediction and observations provides yet more evidence that our simplified freezing model is not a good representative. However, hydrofracturing (e.g. Nicolas 1990; Ceuleneer & Rabinowicz 1992), the formation of veins in areas of high melt/rock ratios (Stevenson 1989), the unstable formation of high-porosity channels as a result of dissolution reactions between the melt and the solid matrix, which increases local porosity (e.g. Kelemen *et al.* 1995a,b; Aharonov *et al.* 1995), and tensile crack formation (Sleep 1984) are amongst the possible mechanisms that can enhance permeability, increase melt velocity and thus reduce the extent of freezing within the decompacting layer. The faster migrating melt would lose less thermal energy and undergo a lesser extent of freezing, resulting in shallow-depth peridotites that are less refertilized than that predicted by our models. To test the validity of this hypothesis, we increase the permeability by a maximum factor of 100 within a layer 6.4 km thick beneath the sloping base of the lithosphere for a model with a half-spreading rate of 50 km Myr^{-1}. The permeability enhancement is at a maximum at the top of the layer and drops quadratically towards the base of the layer. Such an increase of permeability enhances the crustal thickness by about 15 per cent or about 1 km, and reduces freezing by about 30 per cent.

ACKNOWLEDGMENTS

This research was supported by a Natural Sciences and Engineering Research Council of Canada (NSERC) grant to JA-H. AG was partially supported by a scholarship from the Ministry of Culture and Higher Education of Iran. We

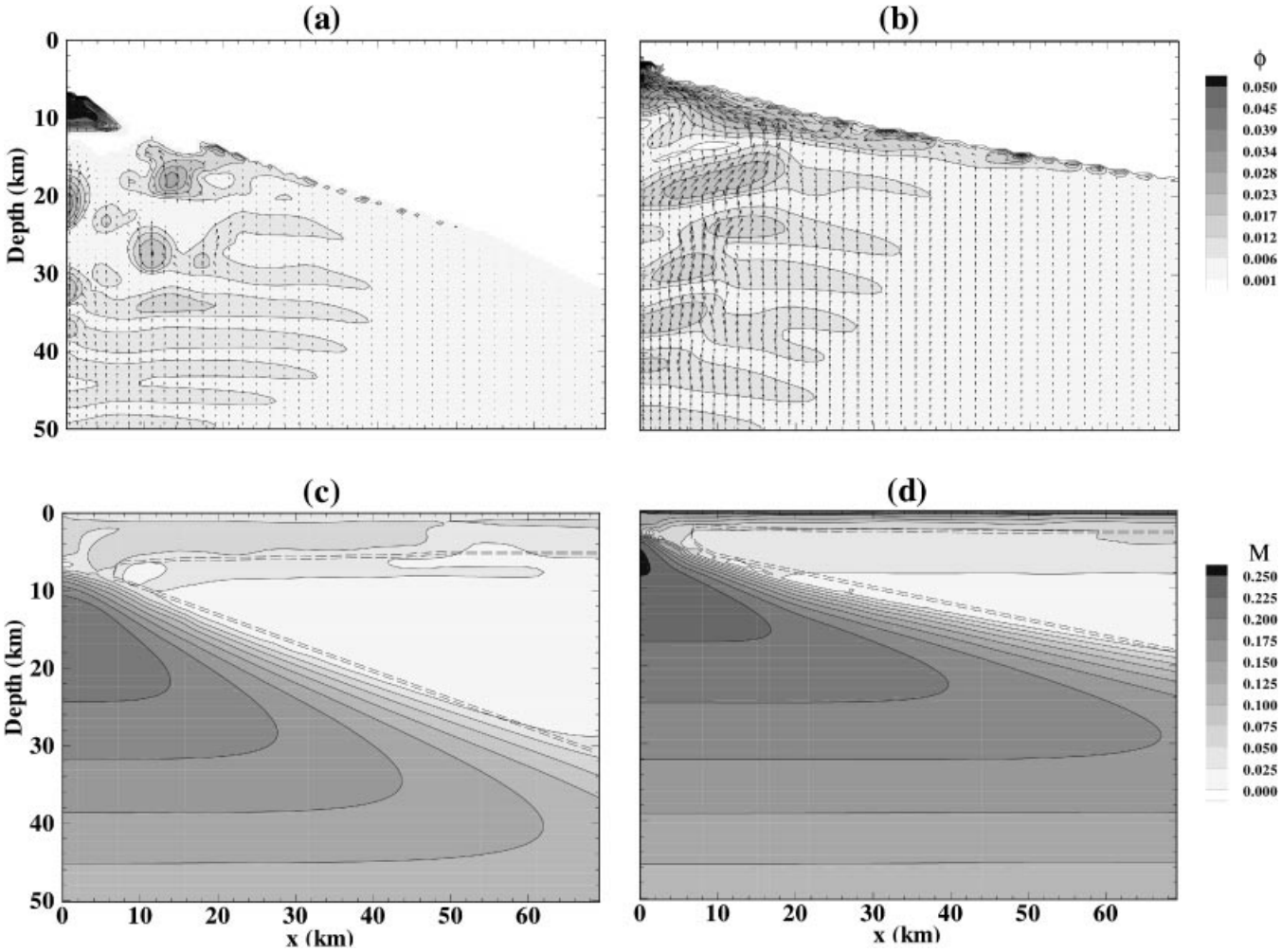

Figure 7. Snapshots of the melt fraction field for (a) a half-spreading rate of 10 km Myr^{-1} and (b) a half-spreading rate of 25 km Myr^{-1}. The melt fraction fields are superimposed by the melt velocity field. For clarity only a quarter of the vector lines are shown in the melt velocity field. (c) and (d) are snapshots of the depletion fields for (a) and (b), respectively, where the dashed curves show part of the freezing layer located close to the ridge axis. Melt extraction regions 5 km wide by 8 km deep and 5 km wide by 6.4 km deep are used for (a) and (b), respectively. A basal temperature of 1425 °C and a melt extraction threshold of 5 per cent are used.

would like to thank Rabi Baliga (Department of Mechanical Engineering, McGill University) for providing us with the SIMPLER single-phase steady-state fluid computation package used in developing our code and Farhad Sobouti for his constructive comments. We would also like to thank Peter Kelemen and an anonymous reviewer for their useful comments.

REFERENCES

Aharonov, E., Whitehead, J.A., Kelemen, P.B. & Spiegelman, M., 1995. Channeling instability of upwelling melt in the mantle, *J. geophys. Res.,* **100,** 20 433–20 450.

Barnouin-Jha, K. & Parmentier, E.M., 1997. Buoyancy mantle upwelling and crustal production at oceanic spreading centers: on-axis segmentation and off-axis melting, *J. geophys. Res.,* **102,** 11 979–11 989.

Buck, W.R. & Su, W., 1989. Focused mantle upwelling below mid-ocean ridges due to feedback between viscosity and melting, *Geophys. Res. Lett.,* **16,** 641–644.

Ceuleneeer, G. & Rabinowicz, M., 1992. Mantle flow and melt migration beneath oceanic ridges: models derived from observations in ophiolites, *Am. Geophys. Un. Geophys. Monogr.,* **71,** 123–154.

Cheadle, M.J., 1993. The physical properties of texturally equilibrated partially molten rocks, *EOS, Trans. Am. geophys. Un.,* **74,** 283.

Chen, Y., 1992. Oceanic crustal thickness versus spreading rate, *Geophys. Res. Lett.,* **19,** 753–756.

Cordery, M.J. & Phipps Morgan, J., 1992. Melting and mantle flow beneath a mid-ocean spreading center, *Earth planet. Sci. Lett.,* **111,** 493–516.

Cordery, M.J. & Phipps Morgan, J., 1993. Convection and modeling at mid-ocean ridges, *J. geophys. Res.,* **98,** 19 477–19 503.

Crane, K., 1985. The spacing of rift axis highs: dependence upon diapiric processes in the underlying asthenosphere?, *Earth planet. Sci. Lett.,* **72,** 405–414.

Dick, H.J.B. & Natland, J.H., 1996. Late-stage melt evolution and transport in the shallow mantle beneath the East Pacific Rise, in *Proc. ODP Sci. Results,* pp. 103–134, eds Mvel, C., Gillis, K.M., Allan, J.F. & Meyer, P.S., ODP, College Station, TX.

Forsyth, D.W. *et al.*, 1998. Imaging the deep seismic structure beneath a mid-ocean ridge: the Melt experiment, *Science,* **280,** 1215–1218.

Ghods, A. & Arkani-Hamed, J., 1998. Effect of melt migration on the dynamics and volume of melt generation of upwelling plumes, *J. geophys. Res,* submitted.

Harding, A.J., Orcutt, J.A., Kappus, M.E., Vera, E.E., Mutter, J.C., Buhl, P., Detrick, R.S. & Brocher, T.M., 1989. Structure of young oceanic crust at 13N on the East Pacific Rise from expanding spread profiles, *J. geophys. Res.,* **94,** 12 163–12 196.

Hirth, G. & Kohlstedt, D.L., 1995a. Experimental constraints on the dynamics of the partially molten upper mantle 2. Deformation in the dislocation creep regime, *J. geophys. Res.,* **100,** 15 441–15 449.

Hirth, G. & Kohlstedt, D.L., 1995b. Experimental constraints on the dynamics of the partially molten upper mantle: deformation in the diffusion creep regime, *J. geophys. Res.,* **100,** 1981–2001.

Hirth, G. & Kohlstedt, D.L., 1996. Water in the oceanic upper mantle: implications for rheology, melt extraction and the evolution of the lithosphere, *Earth planet. Sci. Lett.,* **144,** 93–108.

Huang, P.Y. & Solomon, S.C., 1988. Centriod depths of mid-ocean ridge earthquakes: dependence on spreading rate, *J. geophys. Res.,* **93,** 13 445–13 477.

Jha, K., Parmentier, E.M. & Morgan, J.P., 1994. The role of mantle-depletion and melt-retention buoyancy in spreading-center segmentation, *Earth planet. Sci. Lett.,* **125,** 221–234.

Johnson, K.T.M. & Dick, H.J.B., 1992. Open system melting and temporal and spatial variation of peridotite and basalt at the Atlantis II Fracture Zone, *J. geophys. Res.,* **97,** 9219–9241.

Johnson, K.T.M., Dick, H.J.B. & Shimizu, N., 1990. Melting in the oceanic upper mantle: an ion microprobe study of diopsides in abyssal peridotites, *J. geophys. Res.,* **95,** 2661–2678.

Kelemen, P.B. & Aharonov, E., 1998. Periodic formation of magma fractures and generation of layered gabbros in the lower crust beneath oceanic spreading ridges, in *Faulting and Magmatism at Mid-Ocean Ridges,* pp. 267–289, eds Buck, W.R., Delaney, P.T., Karson, J.A. & Lagabrielle, Y., *Geophys. Monogr.,* Vol. 106, AGU, Washington.

Kelemen, P.B. & Dick, H.J.B., 1995. Focused melt flow and localized deformation in the upper mantle: juxtaposition of replacive dunite and ductile shear zones in the Josephonie peridotite, SW Oregon, *J. geophys. Res.,* **100,** 423–438.

Kelemen, P.B., Shimizu, N. & Salters, V.J.M., 1995a. Extraction of mid-ocean-ridge basalt from the upwelling mantle by focused flow of melt in dunite channels, *Nature,* **375,** 747–753.

Kelemen, P.B., Whitehead, J.A., Aharonov, E. & Jordahl, K.A., 1995b. Experiments on flow focusing in soluble porous media, with applications to melt extraction from the mantle, *J. geophys. Res.,* **100,** 475–496.

Kohlstedt, D.L., 1992. Structure, rheology and permeability of partially molten rocks at low melt fractions, in *Mantle Flow and Melt Generation,* pp. 103–121, eds Phipps Morgan, J., Blackman, D.K. & Sinton, J.M., *Geophys. Monogr.,* Vol. 71, AGU, Washington.

Korenaga, J. & Kelemen, P.B., 1997. Origin of gabbro sills in the Moho transition zone of the Oman ophiolite: implications for magma transport in the oceanic lower crust, *J. geophys. Res.,* **102,** 27 729–27 749.

Macdonald, K.C., 1984. Mid-ocean ridges: fine scale tectonics, volcanic and hydrothermal processes within the plate boundary zone, *Ann. Rev. Earth planet. Phys.,* **10,** 155–190.

McKenzie, D.P., 1984. The generation and compaction of partially molten rock, *J. Petrol.,* **25,** 713–765.

McKenzie, D. & Bickle, M.J., 1988. The volume and composition of melt generated by extension of the lithosphere, *J. Petrol.,* **29,** 625–679.

Nicolas, A., 1990. Melt extraction from mantle peridotites: hydro-fracturing or porous flow consequences on oceanic ridge activity, in *Magma Transport and Storage,* pp. 160–174, ed. Ryan, M.P., Wiley, Chichester.

Patankar, S.V., 1980. *Numerical Heat Transfer and Fluid Flow,* Hemisphere, Washington.

Phipps Morgan, J., 1987. Melt migration beneath mid-ocean spreading centers, *Geophys. Res. Let.,* **14,** 1238–1241.

Prakash, C. & Patankar, S.V., 1985. A control volume-based finite-element method for solving the Navier Stokes equations using equal-order velocity-pressure interpolation, *Numerical Heat Transfer,* **8,** 259–280.

Presnall, D.C. & Walter, M.J., 1993. Melting of forsterite, Mg_2SiO_4, from 9.7 to 16.5 GPa, *J. geophys. Res.,* **98,** 19 777–19 783.

Rabinowicz, M., Nicholas, A. & Vigneresse, J.L., 1984. A rolling mill effect in asthenosphere beneath oceanic spreading centers, *Earth planet. Sci. Lett.,* **67,** 97–108.

Ribe, N.M., 1985. The deformation and compaction of partial molten zones, *Geophys. J. R. astr. Soc.,* **83,** 487–502.

Ross, K. & Elthon, D., 1996. Extreme incompatible trace element depletion of diopside in residual mantle from south of the Kane Fracture Zone, *Proc. ODP, Sci. Res.,* **153,** 277–284.

Sclater, J.G. & Parsons, B., 1981. Oceans and continents: similarities and differences in the mechanisms of heat loss, *J. geophys. Res.,* **86,** 11 535–11 552.

Sinton, J.M. & Detrick, R.S., 1992. Mid-ocean ridge magma chambers, *J. geophys. Res.,* **97,** 197–216.

Sleep, N.H., 1984. Tapping of magmas from ubiquitous mantle hetrogeneities: an alternative to mantle plumes?, *J. geophys. Res.,* **89,** 10 029–10 041.

Sotin, C. & Parmentier, E.M., 1989. Dynamical consequences of compositional and thermal density stratification beneath spreading centers, *Geophys. Res. Lett.,* **16,** 835–838.

Sparks, D.W. & Parmentier, E.M., 1991. Melt extraction from the mantle beneath oceanic spreading centers, *Earth planet. Sci. Lett.,* **105,** 368–377.

Sparks, D.W. & Parmentier, E.M., 1994. The generation and migration of partial melt beneath oceanic spreading centers, in *Magmatic System,* pp. 55–76, ed. Ryan, M.P., Academic, San Diego.

Spiegelman, M., 1993. Flow in deformable porous media. Part 2, simple analysis, *J. Fluid Mech.,* **247,** 39–63.

Stein, C.A. & Stein, S., 1992. A model for the global variation in oceanic depth and heat flow with lithospheric age, *Nature,* **359,** 123–129.

Stevenson, D.J., 1989. Spontaneous small-scale melt segregation in partial melts undergoing deformation, *Geophys. Res. Lett.,* **9,** 1064–1070.

Sweby, P.K., 1984. High resolution schemes using flux limiters for hyperbolic conservation laws, *SIAM J. Numer. Anal.,* **21,** 995–1001.

Tisseau, C. & Tonnerre, T., 1995. Non steady-state thermal model of spreading ridges: implications for melt generation and mantle outcrops, in *Mantle and Lower Crust Exposed in Oceanic Ridges and in Ophiolites,* pp. 181–214, eds Vissers, R.L.M & Nicolas, A., Proc. Symp., Kluwer, Strasbourg.

Turcotte, D.L. & Phipps Morgan, J., 1992. The physics of magma migration and mantle flow beneath a mid-ocean ridge, in *Mantle Flow and Melt Generation at Mid-Ocean Ridges,* pp. 155–182, eds Phipps Morgan, J., Blackman, D.K. & Sinton, J.M., *Geophys. Monogr.,* Vol. 71, AGU, Washington.

Vera, E.E., Mutter, J.C., Buhl, P., Orcutt, J.A., Harding, A.J., Kappus, M.E., Detrick, R.S. & Brocher, T.M., 1990. The structure of 0- to 0.2-m.y.-old oceanic crust at 9N on the East Pacific Rise from expanded spread profiles, *J. geophys. Res.,* **95,** 15 529–15 556.

Von Bargen, N. & Waff, H.S., 1986. Permeabilities, interfacial areas and curvatures of partially molten systems: results of numerical computations of equilibrium microstructures, *J. geophys. Res.,* **91,** 9261–9276.

Whitehead, J.A., Dick, H.J.B. & Schouten, H., 1984. A mechanism for magmatic accretion under spreading centers, *Nature,* **312,** 146–148.